Comparison Between Modal Analysis and Impedance-based Methods for Analysing Stability of Unbalanced Microgrids with Grid-forming Electronic Power Converters

Sauro J. Yague, *Member*, *IEEE*, Aurelio García-Cerrada, *Senior Member*, *IEEE*, and Pere Palacín Farré

***Abstract*—Stability in unbalanced power systems has deserved little attention in the literature. Given the importance of this scenario in distribution systems with distributed generation, this paper revisits modal analysis techniques for stability studies in power systems, and explains how to tackle unbalanced power systems with voltage-dependent loads. The procedure is described in detail and applied to a low-voltage (LV) simple case study with two grid-forming electronic power converters and unbalanced loads. Results are then compared with those obtained with the popular impedance-based method. While the latter is easier to implement using simulation or field data, the former requires complete information of the system, but gives a better insight into the problem. Since both methods are based on a small-signal approximation of the system, they provide similar results, but they discern different information. A larger second case study based on an LV CIGRE distribution system is also analysed. Results are obtained using a detailed Simulink model of the microgrids with electronic power converters.**

***Index Terms*—Stability, microgrid, modal analysis, impedance-based method, unbalanced distribution system.**

I. Introduction

In response to the global climate change caused by the excessive atmospheric concentration of carbon dioxide and other greenhouse gases, the penetration of renewable energy sources (RESs) into power systems has been soaring worldwide. When RESs (mainly wind and solar) are used, electronic power converters are required to interface energy generation with the power system, providing fast control of active and reactive power. Nowadays, electronic power converters for grid applications are mainly voltage source converters (VSCs), which can be of two types: grid-forming (GFo) VSCs that control output voltage and frequency at their filter output, and grid-following (GFl) VSCs that control the magnitude and orientation of their filter output current with respect to the voltage at the point of coupling (PoC). In GFo-VSCs, an inner current loop is often used to deal better with possible resonances of the output filter and to provide means of limiting the output current of the converter. GFl-VSCs require a phase-lock-loop (PLL) to synchronize with the power system by tracking the voltage angle at the converter connection bus. Current limiting can be provided naturally. A comprehensive review of the control of VSCs and their main characteristics is presented in [1].

Modal analysis is considered the standard tool to characterise small-signal stability of traditional power systems described in a synchronously-rotating {*dq*} reference frame, after Park's transformation [2]. Three-phase sinusoidal variables are transformed into two constant components {*dq*} in steady state, plus the nearly-always forgotten zero component (sometimes called "homopolar"). Under these circumstances, the non-linear model of the power system can be linearised at a steady-state operation point. The eigenvalues of the linearised power system equations give information of the system dynamics; participation factors of eigenvalues in state variables give information of which state variables are affected by relevant and less-relevant dynamics [3]; and sensitivities of those eigenvalues can be used to design, for example, power system stabilisers to tackle dangerous power oscillations for conventional synchronous generators [4], [5] or for VSCs [6].

In conventional power systems, power line dynamics are generally neglected, because the dynamics of high-inertia rotating machines and their controls are considerably slower than those of the lines. However, in microgrids, fast control of inertia-less VSCs or VSCs with virtual inertia may render line dynamics to be relevant. This will tend to increase the size and complexity of case-study models. Nevertheless, the application of modal analysis to balanced microgrids has been the subject of previous research efforts. For example,

Manuscript received: October 14, 2022; revised: January 5, 2023; accepted: February 27, 2023. Date of CrossCheck: February 27, 2023. Date of online publication: April 5, 2023.

This work has been partially supported by Comunidad de Madrid, the European Social Fund and the European Regional Development Fund ("ERDF a way of making Europe") under the research programme of activities PROMINT-CM with Ref. S2018/EMT-4366.

S. J. Yague and P. P. Farré are with IQS School of Engineering, Ramón Llull University, Via Augusta 390, 08017 Barcelona, Spain (e-mail: sauro.yague@iqs.url.edu; pere.palacin@iqs.url.edu).

A. García-Cerrada (corresponding author) is with Institute for Research in Technology, ICAI School of Engineering, Comillas Pontifical University, Alberto Aguilera 23, 28015 Madrid, Spain (e-mail: aurelio@comillas.edu).

DOI: 10.35833/MPCE.2022.000669

[7] investigates the interactions among VSCs and the network dynamics, and it analyses the stability of a microgrid case study for different droop gains in the VSCs. Reference [8] studies the stability of an islanded hybrid alternating current (AC)/direct current (DC) microgrid with a bidirectional interlink converter with a droop-based control algorithm. Network frequency and bus voltage in the AC section, and bus voltage at the DC section, are maintained within permissible limits. Reference [9] proposes a generalised framework for small-signal stability analysis for microgrids with primary and secondary distributed controls based on multi-agents, considering communication latency and uncertainty. In [10], a sensitivity analysis is carried out to check whether it is possible to prevent the instability of a microgrid when operated with constant power loads (induction motors), by tuning the internal voltage and current controller gain values of GFo-VSCs. In all microgrid-related cases in the literature, system and loads are considered balanced, like in conventional power systems.

So far, the application of modal analysis in traditional power systems and in microgrids relies on finding the steady-state operation point by making the derivatives of the state variables equal zero and solving the resulting system of non-linear equations. However, unlike in the analysis of conventional power systems, loads in microgrids are often unbalanced, and straight application of Park's transformation does not give constant state variables in steady state. Therefore, the usual linearisation of non-linear power system models is not possible. However, experts suggest that "unbalance" should not be neglected when studying stability in microgrids [11], [12], which rules out the use of a traditional $\{dq\}$ model.

A modified Park's transformation for unbalanced power systems has been proposed in [13]. In a general case, this transformation applied to a three-phase system renders d, q, and 0 components for a positive (+) and a negative (−) sequence, i.e., a total of six state variables d^+, q^+, 0^+, d^-, q^-, 0^-, but only four of them are constant in steady state ($d^\pm$ and $q^\pm$), while the zero components ($0^\pm$) have oscillations of the fundamental frequency. Therefore, this method cannot always be used for a traditional modal analysis. In the cases in [13], zero current components ($0^\pm$) are all zero and are ignored.

This paper brings three contributions to this scenario.

1) It presents a modification applied to [13] in order to always have constant $\{dq0^\pm\}$ components in steady state, which is the necessary step to have constant state variables at an operation point in steady state, and obtain small-signal linear approximations of non-linear unbalanced power systems.

2) It provides a comparison between modal stability analysis and the impedance-based method, since the latter is popular in converters connected to grids or microgrids [14], but has not been applied to unbalanced power systems. Impedance-based analysis also relies on a linear model derived at a constant operation point and it is ideal for the analysis and design of a single converter to be connected to a grid using a reduced model of the latter. Modal techniques can address a system-based analysis, providing richer information.

3) Finally, the paper computes active and reactive power in unbalanced power systems based on constant $\{dq0^\pm\}$ components in steady state.

The analysis tools including details of the modified Park's transformation and the principles of modal analysis and of impedance-based stability analysis are presented in Section II. The calculation of active and reactive power using the proposed transformation is presented in Section II-F. The dynamic model of a microgrid with GFo-VSCs using $\{dq0^\pm\}$ components will be discussed in Section III. Two case studies [15] will be analysed in Section IV. Finally, conclusions will be summarized in Section V.

II. Analysis Tools

A. Modified Park's Transformation for Unbalanced Microgrids

The analysis that follows is based on [13], but it goes a step further. Let us consider the following matrices:

$$\boldsymbol{T}_\theta^+ = \overbrace{\begin{bmatrix} \cos\theta & \sin\theta & 0 \\ -\sin\theta & \cos\theta & 0 \\ 0 & 0 & 1 \end{bmatrix}}^{\boldsymbol{T}_{dq0}^+} \cdot \sqrt{\frac{2}{3}} \overbrace{\begin{bmatrix} 1 & -\frac{1}{2} & -\frac{1}{2} \\ 0 & \frac{\sqrt{3}}{2} & -\frac{\sqrt{3}}{2} \\ \frac{1}{\sqrt{2}} & \frac{1}{\sqrt{2}} & \frac{1}{\sqrt{2}} \end{bmatrix}}^{\boldsymbol{T}_{\alpha\beta\gamma}} \tag{1}$$

where $\theta=\omega t$, ω is the frequency of the power system; t is the time; and $\boldsymbol{T}_\theta^+$ is the traditional power-invariant Park's transformation used in three-phase systems.

Under unbalanced conditions, a phase k of any three-phase (abc) electrical variable $\boldsymbol{x}_{abc}(t)$ ($\boldsymbol{x}_{abc}$ will be either a voltage $\boldsymbol{v}$ or a current $\boldsymbol{i}$ column vector with components a, b, and c) can be written as:

$$\begin{aligned} x_k(t) = {} & \sqrt{2}\,X_0\cos(\omega t+\varphi_0) + \sqrt{2}\,X_+\cos(\omega t+\varphi_+ +\sigma) + \\ & \sqrt{2}\,X_-\cos(\omega t+\varphi_- -\sigma) \end{aligned} \tag{2}$$

where $\sigma=0$, $\sigma=-\frac{2\pi}{3}$, $\sigma=\frac{2\pi}{3}$ for phases a, b, and c, respectively; $\{X_0, X_+, X_-\}$ are the root-mean-square (RMS) values; and $\{\varphi_0, \varphi_+, \varphi_-\}$ are the arbitrary initial phase displacements of the so-called homopolar (0), positive, and negative sequence components of $\boldsymbol{x}_{abc}(t)$, respectively.

If (1) is applied to $\boldsymbol{x}_{abc}(t)$ with components as in (2), one obtains (3) and (4), proving that, in general, the so-called $\{dq0\}$ components of variable $\boldsymbol{x}_{abc}$ do not remain constant in steady state.

$$\overbrace{[x_d(t), x_q(t), x_0(t)]^{\mathrm{T}}}^{\boldsymbol{x}_{dq0}} = \boldsymbol{T}_\theta^+ \overbrace{[x_a(t), x_b(t), x_c(t)]^{\mathrm{T}}}^{\boldsymbol{x}_{abc}} \tag{3}$$

$$\begin{bmatrix} x_d(t) \\ x_q(t) \\ x_0(t) \end{bmatrix} = \begin{bmatrix} \sqrt{3}\,X_+\cos\varphi_+ + \sqrt{3}\,X_-\cos(2\omega t+\varphi_-) \\ \sqrt{3}\,X_+\sin\varphi_+ - \sqrt{3}\,X_-\sin(2\omega t+\varphi_-) \\ \sqrt{6}\,X_0\cos(\omega t+\varphi_0) \end{bmatrix} \tag{4}$$

Reference [13] modifies Park's transformation as follows:

$$\boldsymbol{x}^{\pm}_{dq0\omega} = \boldsymbol{T}(t)\begin{bmatrix} \boldsymbol{x}_{abc}(t) \\ \boldsymbol{x}_{abc}(t-T/4) \end{bmatrix} \tag{5}$$

$$\boldsymbol{x}^{\pm}_{dq0\omega} = [x^{+}_{d\omega}, x^{+}_{q\omega}, x^{+}_{0\omega}, x^{-}_{d\omega}, x^{-}_{q\omega}, x^{-}_{0\omega}]^{\mathrm{T}} \tag{6}$$

$$\boldsymbol{T}(t) = \tilde{\boldsymbol{T}}_{dq0}(t)\boldsymbol{T}_{+-0}\tilde{\boldsymbol{T}}_{\alpha\beta\gamma}(t) \tag{7}$$

where $T = 2\pi/\omega$. The following 6×6 matrices are given:

$$\begin{cases} \tilde{\boldsymbol{T}}_{dq0}(t) = \begin{bmatrix} \boldsymbol{T}^{+}_{dq0} & \boldsymbol{0}_{3\times 3} \\ \boldsymbol{0}_{3\times 3} & \boldsymbol{T}^{-}_{dq0} \end{bmatrix} \\ \tilde{\boldsymbol{T}}_{\alpha\beta\gamma}(t) = \begin{bmatrix} \boldsymbol{T}_{\alpha\beta\gamma} & \boldsymbol{0}_{3\times 3} \\ \boldsymbol{0}_{3\times 3} & \boldsymbol{T}_{\alpha\beta\gamma} \end{bmatrix} \end{cases} \tag{8}$$

where $\boldsymbol{0}_{3\times 3}$ is a 3×3 zero matrix; $\boldsymbol{T}^{-}_{dq0}(\theta) = \boldsymbol{T}^{+}_{dq0}(-\theta)$; and $\boldsymbol{T}_{+-0}$ is given as:

$$\boldsymbol{T}_{+-0} = \frac{1}{2}\begin{bmatrix} 1 & 0 & 0 & 0 & -1 & 0 \\ 0 & 1 & 0 & 1 & 0 & 0 \\ 0 & 0 & 1 & 0 & 0 & 0 \\ 1 & 0 & 0 & 0 & 1 & 0 \\ 0 & 1 & 0 & -1 & 0 & 0 \\ 0 & 0 & 0 & 0 & 0 & 1 \end{bmatrix} \tag{9}$$

In the 6×1 column vector $\boldsymbol{x}^{\pm}_{dq0\omega}$ in (5), the first, second, forth, and fifth elements are constant in steady state, while the third and sixth ones are not. A constant column vector $\boldsymbol{x}^{\pm}_{dq0}$ can be obtained as $\boldsymbol{x}^{\pm}_{dq0} = [x^{+}_{d}, x^{+}_{q}, x^{+}_{0}, x^{-}_{d}, x^{-}_{q}, x^{-}_{0}]^{\mathrm{T}}$, if:

$$[x^{+}_{d}, x^{+}_{q}, x^{-}_{d}, x^{-}_{q}]^{\mathrm{T}} = [x^{+}_{d\omega}, x^{+}_{q\omega}, x^{-}_{d\omega}, x^{-}_{q\omega}]^{\mathrm{T}} \tag{10}$$

$$\begin{bmatrix} x^{+}_{0} \\ x^{-}_{0} \end{bmatrix} = \begin{bmatrix} x^{+}_{0\omega}\cos\theta + x^{-}_{0\omega}\sin\theta \\ -x^{+}_{0\omega}\sin\theta + x^{-}_{0\omega}\cos\theta \end{bmatrix} \tag{11}$$

For a one-step transformation, $\boldsymbol{T}(t)$ in (5) changes to $\hat{\boldsymbol{T}}(t)$:

$$\hat{\boldsymbol{T}}(t) = \begin{bmatrix} 1 & 0 & 0 & 0 & 0 & 0 \\ 0 & 1 & 0 & 0 & 0 & 0 \\ 0 & 0 & \cos\theta & 0 & 0 & \sin\theta \\ 0 & 0 & 0 & 1 & 0 & 0 \\ 0 & 0 & 0 & 0 & 1 & 0 \\ 0 & 0 & -\sin\theta & 0 & 0 & \cos\theta \end{bmatrix}\boldsymbol{T}(t) \tag{12}$$

Applying (12) to (2) ($k = a, b, c$) gives:

$$\boldsymbol{x}^{\pm}_{dq0} = \begin{bmatrix} \boldsymbol{x}^{+}_{dq0} \\ \boldsymbol{x}^{-}_{dq0} \end{bmatrix} = \begin{bmatrix} [x^{+}_{d}, x^{+}_{q}, x^{+}_{0}]^{\mathrm{T}} \\ [x^{-}_{d}, x^{-}_{q}, x^{-}_{0}]^{\mathrm{T}} \end{bmatrix} \tag{13}$$

which is a 6×1 constant vector with:

$$\boldsymbol{x}^{+}_{dq0} = \sqrt{3}\left[X_{+}\cos\varphi_{+}, X_{+}\sin\varphi_{+}, \frac{X_0}{\sqrt{2}}\cos\varphi_0\right]^{\mathrm{T}} \tag{14}$$

$$\boldsymbol{x}^{-}_{dq0} = \sqrt{3}\left[X_{-}\cos\varphi_{-}, -X_{-}\sin\varphi_{-}, \frac{X_0}{\sqrt{2}}\sin\varphi_0\right]^{\mathrm{T}} \tag{15}$$

B. {dq0$^{\pm}$} Model of a Series Unbalanced RL Circuit

The differential equations for a star-connected unbalanced RL load, with neutral point connected to ground through an impedance L_n and R_n (see Fig. 1), can be written as (16). In Fig. 1, $i_k(t)$ ($k = a, b, c$) is the load current; $v_k(t)$ is the phase voltage to ground; R_k is the per-phase load resistance; L_k is the per-phase load inductance; and $V_n(t)$ and $i_n(t)$ are the neutral voltage and neutral current to ground, respectively.

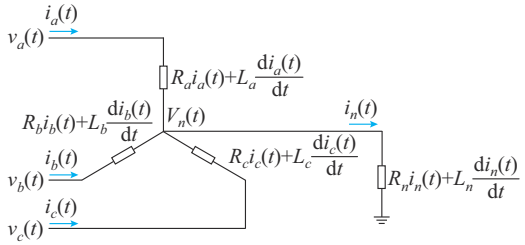

Fig. 1. Unbalanced RL circuit.

$$\begin{bmatrix} \boldsymbol{v}_{abc}(t) \\ \boldsymbol{v}_{abc}\left(t-\frac{T}{4}\right) \end{bmatrix} = \hat{\boldsymbol{R}}_{abc}\begin{bmatrix} \boldsymbol{i}_{abc}(t) \\ \boldsymbol{i}_{abc}\left(t-\frac{T}{4}\right) \end{bmatrix} + \hat{\boldsymbol{L}}_{abc}\begin{bmatrix} \frac{\mathrm{d}}{\mathrm{d}t}\boldsymbol{i}_{abc}(t) \\ \frac{\mathrm{d}}{\mathrm{d}t}\boldsymbol{i}_{abc}\left(t-\frac{T}{4}\right) \end{bmatrix} \tag{16}$$

$$\begin{cases} \hat{\boldsymbol{R}}_{abc} = \begin{bmatrix} \boldsymbol{R}_{abc} & \boldsymbol{0}_{3\times 3} \\ \boldsymbol{0}_{3\times 3} & \boldsymbol{R}_{abc} \end{bmatrix} \\ \hat{\boldsymbol{L}}_{abc} = \begin{bmatrix} \boldsymbol{L}_{abc} & \boldsymbol{0}_{3\times 3} \\ \boldsymbol{0}_{3\times 3} & \boldsymbol{L}_{abc} \end{bmatrix} \end{cases} \tag{17}$$

where $\boldsymbol{R}_{abc}$ and $\boldsymbol{L}_{abc}$ can be built substituting $\S$ by R and L, respectively, in (18):

$$\boldsymbol{R}_{abc} \text{ or } \boldsymbol{L}_{abc} = \begin{bmatrix} \S_a + \S_n & \S_n & \S_n \\ \S_n & \S_b + \S_n & \S_n \\ \S_n & \S_n & \S_c + \S_n \end{bmatrix} \tag{18}$$

Applying (5) (with $\hat{\boldsymbol{T}}(t)$) to (16) yields:

$$\boldsymbol{v}^{\pm}_{dq0} = [\boldsymbol{BB}]\boldsymbol{i}^{\pm}_{dq0} + [\boldsymbol{AA}]\frac{\mathrm{d}}{\mathrm{d}t}\boldsymbol{i}^{\pm}_{dq0} \tag{19}$$

$$[\boldsymbol{BB}] = \left[\hat{\boldsymbol{T}}\hat{\boldsymbol{R}}_{abc}\cdot\hat{\boldsymbol{T}}^{-1} + \hat{\boldsymbol{T}}\hat{\boldsymbol{L}}_{abc}\frac{\mathrm{d}}{\mathrm{d}\theta}[\hat{\boldsymbol{T}}^{-1}]w\right] \tag{20}$$

$$[\boldsymbol{AA}] = [\hat{\boldsymbol{T}}\hat{\boldsymbol{L}}_{abc}\hat{\boldsymbol{T}}^{-1}] \tag{21}$$

Both [$\boldsymbol{BB}$] and [$\boldsymbol{AA}$] are 6×6 matrices of real numbers and are not angle θ dependent.

Often, loads are either connected between two phases or from a phase to ground. These two cases deserve special attention. In a load connected between two phases (a and b, for example), we have:

$$\begin{cases} i_a(t) = -i_b(t) \\ i_c(t) = 0 \end{cases} \tag{22}$$

The application of the transformation in (5) (with $\hat{\boldsymbol{T}}(t)$) gives $i^{+}_0 = 0$, $i^{-}_0 = 0$, and (23) is obtained.

$$[\boldsymbol{i}^{-}_{dq}] = \frac{1}{2}\begin{bmatrix} 1 & \sqrt{3} \\ \sqrt{3} & -1 \end{bmatrix}[\boldsymbol{i}^{+}_{dq}] \tag{23}$$

where $[\boldsymbol{i}^{-}_{dq}] = [i^{-}_{d}, i^{-}_{q}]^{\mathrm{T}}$ and $[\boldsymbol{i}^{+}_{dq}] = [i^{+}_{d}, i^{+}_{q}]^{\mathrm{T}}$; which means that, out of the six state variables in (13), only two are left.

If (5) (with $\hat{\boldsymbol{T}}(t)$) is applied to a two-phase unbalanced load connected to ground (phases a and b, for example):

$$\begin{cases} i_a(t) + i_b(t) = i_n(t) \\ i_c(t) = 0 \end{cases} \tag{24}$$

$$[\boldsymbol{i}_0^{\pm}]=\begin{bmatrix} \frac{\sqrt{2}}{4} & \frac{\sqrt{6}}{4} & \frac{\sqrt{2}}{4} & \frac{\sqrt{6}}{4} \\ -\frac{\sqrt{6}}{4} & \frac{\sqrt{2}}{4} & \frac{\sqrt{6}}{4} & -\frac{\sqrt{2}}{4} \end{bmatrix}\begin{bmatrix} \boldsymbol{i}_{dq}^{+} \\ \boldsymbol{i}_{dq}^{-} \end{bmatrix} \tag{25}$$

which results in a fourth-order dynamic system.

Finally, one phase connected to ground with an impedance gives:

$$\begin{cases} i_a(t)=i_n(t) \\ i_b(t)=i_c(t)=0 \end{cases} \tag{26}$$

$$\begin{bmatrix} \boldsymbol{i}_0^{\pm} \\ \boldsymbol{i}_{dq}^{-} \end{bmatrix}=\begin{bmatrix} \frac{\sqrt{2}}{2} & 0 & 1 & 0 \\ 0 & \frac{\sqrt{2}}{2} & 0 & -1 \end{bmatrix}^{\mathrm{T}}[\boldsymbol{i}_{dq}^{+}] \tag{27}$$

which results in a second-order system, again.

Similarly, a $\{dq0^{\pm}\}$ model of a parallel unbalanced *RC* circuit should be derived to include the bus voltage dynamics.

C. $\{dq0^{\pm}\}$ Impedance Analysis

The $\{dq0^{\pm}\}$ impedance matrix for the circuit in Fig. 1 can be computed by transforming (19) into the frequency domain using Laplace transform, resulting in a 6×6 impedance matrix of the form:

$$\boldsymbol{Z}_{dq0}(s)=[\boldsymbol{BB}]+[\boldsymbol{AA}]s=\begin{bmatrix} \boldsymbol{Z}_{dq0}^{++}(s) & \boldsymbol{Z}_{dq0}^{+-}(s) \\ \boldsymbol{Z}_{dq0}^{-+}(s) & \boldsymbol{Z}_{dq0}^{--}(s) \end{bmatrix} \tag{28}$$

where $\boldsymbol{Z}_{dq0}(s)$ has been divided into four 3×3 transfer-function matrices. $\boldsymbol{Z}_{dq0}(s)$ has been calculated for $s=\mathrm{j}2\pi\times50$ in the balanced and unbalanced cases (cases 0 and 1, respectively), as shown in Table I, and the results are given in Tables II and III, respectively.

TABLE I
SERIES RL CIRCUIT CASES

Case	Parameters
0	$R_a=R_b=R_c=10\ \Omega,\ L_a=L_b=L_c=100$ mH
1	$R_a=10\ \Omega, R_b=20\ \Omega, R_c=30\ \Omega, L_a=400$ mH, $L_b=500$ mH, $L_c=600$ mH
0 and 1	$R_n=1\ \Omega,\ L_n=10$ mH

As expected, in the balanced case (Table II), the positive-, negative-, and homopolar-sequences are decoupled, while in the unbalanced case (Table III), the three sequences are coupled, which, if neglected, may result in an incorrect stability assessment.

D. Modal Analysis and Participation Factors

For a linear time-invariant system described by a state-variable model, with $\boldsymbol{A}\in\mathbf{R}^{n\times n}$:

$$\dot{\boldsymbol{x}}(t)=\boldsymbol{A}\boldsymbol{x}(t)+\boldsymbol{B}\boldsymbol{u} \tag{29}$$

The eigen-analysis of matrix $\boldsymbol{A}$ will produce n eigenvalues λ_i ($1\le i\le n$). Assuming that $\lambda_i\ne\lambda_j$ if $i\ne j$, each λ_i will have a column left eigenvector $\boldsymbol{w}_i$ associated ($\boldsymbol{w}_i^{\mathrm{T}}\boldsymbol{A}=\lambda_i\boldsymbol{w}_i^{\mathrm{T}}$), with elements w_i^j ($1\le j\le n$) and a column right eigenvector $\boldsymbol{v}_i$ ($\boldsymbol{A}\boldsymbol{v}_i=\lambda_i\boldsymbol{v}_i$) with elements v_i^j ($1\le j\le n$).

TABLE II
CASE 0: IMPEDANCE MATRIX

Matrix	Value
$\boldsymbol{Z}_{dq0}^{++}$	$\begin{bmatrix} 10.00+\mathrm{j}31.41 & -31.41 & 0 \\ 31.41 & 10.00+\mathrm{j}31.41 & 0 \\ 0 & 0 & 13.00+\mathrm{j}40.84 \end{bmatrix}$
$\boldsymbol{Z}_{dq0}^{+-}$	$\begin{bmatrix} 0 & 0 & 0 \\ 0 & 0 & 0 \\ 0 & 0 & -40.84 \end{bmatrix}$
$\boldsymbol{Z}_{dq0}^{-+}$	$\begin{bmatrix} 0 & 0 & 0 \\ 0 & 0 & 0 \\ 0 & 0 & 40.84 \end{bmatrix}$
$\boldsymbol{Z}_{dq0}^{--}$	$\begin{bmatrix} 10.00+\mathrm{j}31.41 & 31.41 & 0 \\ -31.41 & 10.00+\mathrm{j}31.41 & 0 \\ 0 & 0 & 13.00+\mathrm{j}40.84 \end{bmatrix}$

TABLE III
CASE 1: IMPEDANCE MATRIX

Matrix	Value
$\boldsymbol{Z}_{dq0}^{++}$	$\begin{bmatrix} 20.00+\mathrm{j}157.08 & -157.08 & 5.75-\mathrm{j}22.21 \\ 157.08 & 20.00+\mathrm{j}157.08 & -26.30-\mathrm{j}12.83 \\ -9.95-\mathrm{j}11.11 & 9.07-\mathrm{j}6.41 & 23.00+\mathrm{j}166.50 \end{bmatrix}$
$\boldsymbol{Z}_{dq0}^{+-}$	$\begin{bmatrix} -14.07-\mathrm{j}15.71 & -12.82+\mathrm{j}9.07 & 26.30+\mathrm{j}12.83 \\ -12.82+\mathrm{j}9.07 & 14.07+\mathrm{j}15.71 & 5.75-\mathrm{j}22.21 \\ 2.88-\mathrm{j}11.11 & -13.15-\mathrm{j}6.41 & -166.50 \end{bmatrix}$
$\boldsymbol{Z}_{dq0}^{-+}$	$\begin{bmatrix} 4.07-\mathrm{j}15.71 & 18.59+\mathrm{j}9.07 & -19.90-\mathrm{j}22.21 \\ 18.59+\mathrm{j}9.07 & -4.07+\mathrm{j}15.71 & 18.13-\mathrm{j}12.83 \\ -9.07+\mathrm{j}6.41 & -9.95-\mathrm{j}11.11 & 166.50 \end{bmatrix}$
$\boldsymbol{Z}_{dq0}^{--}$	$\begin{bmatrix} 20.00+\mathrm{j}157.08 & 157.08 & 18.13-\mathrm{j}12.83 \\ -157.08 & 20.00+\mathrm{j}157.08 & 19.90+\mathrm{j}22.21 \\ -13.15-\mathrm{j}6.41 & -2.88+\mathrm{j}11.11 & 23.00+\mathrm{j}166.50 \end{bmatrix}$

The free response of a linear system as (29), given a column vector of initial conditions $\boldsymbol{x}(0)$ is:

$$\boldsymbol{x}(t)=\sum_{i=1}^{n}\boldsymbol{w}_i^{\mathrm{T}}\boldsymbol{x}(0)\mathrm{e}^{\lambda_i t}\boldsymbol{v}_i \tag{30}$$

which, for a given state variable x^j (the j^{th} element in state vector $\boldsymbol{x}(t)$) and initial conditions $x^k=0$ if $k\ne m$ and $x^m=1$ (the m^{th} element in state vector $\boldsymbol{x}(t)$), gives:

$$x^j(t)=w_1^m\mathrm{e}^{\lambda_1 t}v_1^j+w_2^m\mathrm{e}^{\lambda_2 t}v_2^j+\ldots+w_k^m\mathrm{e}^{\lambda_k t}v_k^j+\ldots \tag{31}$$

Based on (31), [16] defines the product $w_i^m v_i^j$ as the participation of λ_i in variable x^j with the initial conditions described above, although participation factors are given more attention for $m=j$. This definition renders complex numbers for the participation factors in a general case, and [17] suggests the following definition for the participation factor of eigenvalue λ_i in state $x^j(t)$, to have "real" participations:

$$p_{ji}=\frac{\left|w_i^j\right|\left|v_i^j\right|}{\sum_{\forall k}\left|w_i^k\right|\left|v_i^k\right|}\Rightarrow\sum_{\forall j}p_{ji}=1 \tag{32}$$

If the power system equations are linearised, the eigenval-

ues of the approximate linear system can be used to study the small-signal stability of the system, while the participation factors can be used to study which states are associated with a given mode (eigenvalue). The system will be stable if all eigenvalues have negative real parts.

This method of analysis can address one VSC connected to the reduced model of the grid, if the parameters of both systems are known, or a more complex system with several VSCs connected through power lines and/or cables.

E. Impedance-based Method for Stability Analysis

The impedance-based method for stability analysis reduces a GFo-VSC and its connected system into an equivalent source and load impedance (as depicted in Fig. 2). Formulated initially by [18] for DC converters, the stability issue is resolved applying Nyquist stability criterion to the resulting impedance ratio. Later on, [19] has extended the stability study for balanced three-phase AC systems applying the generalized Nyquist stability criterion [20] on the product of the converter output impedance (Z_o) and the grid input admittance (Y_g) (with voltages and currents having two components: d and q). Since this method is meant to analyse one converter against the rest of the grid, which might contain more VSCs, possible interactions among converters will remain hidden. However, unlike the one based on modal analysis, this method does not require a detailed model of the system, and the necessary impedances can be calculated either by simulation or by direct experimental measurements. In both cases, a disturbance has to be used, as illustrated by ΔI_p in Fig. 2, where V_T and Z_o are the elements of Thévenin equivalent of the converter under study (voltage and output impedance, respectively); Y_g and I_N are the Norton equivalents which model the admittance and current source of the grid, respectively; and ΔI_p is a test disturbance.

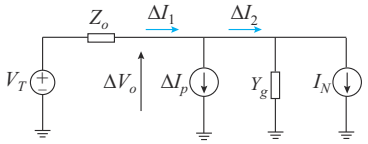

Fig. 2. Perturbation circuit at PoC.

The method is applied to a balanced three-phase AC system with a GFo-VSC and a constant power load in [21]. When primary frequency and/or voltage droop are used for active- and/or reactive-power sharing, the voltage and current variations of ΔV_0 and ΔI_2 in Fig. 2 are partially due to the action of those droops, and [22] suggests a representation similar to the one in Fig. 3 to highlight the influence of the frequency variation on the output of droop-controlled converters. Here, unlike in [22], $Z_o(s)$ is defined as the usual output impedance of the device on the left-hand side of Fig. 2. In Fig. 2, one can write:

$$Z_o(s) = -\frac{\Delta V_o}{\Delta I_1} = -\frac{\Delta V_o}{\Delta I_p}\left[\frac{\Delta I_1}{\Delta I_p}\right]^{-1} \tag{33}$$

$$Y_g(s) = \frac{\Delta I_2}{\Delta V_o} = \frac{\Delta I_2}{\Delta I_p}\left[\frac{\Delta V_o}{\Delta I_p}\right]^{-1} \tag{34}$$

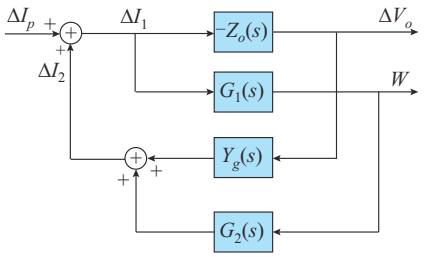

Fig. 3. Block diagram at PoC where blocks contain transfer-functions.

$$G_1(s) = \frac{\Delta w}{\Delta I_1} = \frac{\Delta w}{\Delta I_p}\left[\frac{\Delta I_1}{\Delta I_p}\right]^{-1} \tag{35}$$

$$G_2(s) = \frac{\Delta I_2}{\Delta w} = \frac{\Delta I_2}{\Delta I_p}\left[\frac{\Delta w}{\Delta I_p}\right]^{-1} \tag{36}$$

Reference [22] demonstrates that the stability of the whole system can be studied applying the generalized Nyquist criterion to the matrix of open-loop transfer functions $L(s)$ shown in (37), i.e., the system will be stable if the loci of the eigenvalues of $L(j\omega)$ $(-\infty \le \omega < \infty)$ do not encircle the point $(-1, 0)$ in the complex plane.

$$L(s) = Y_g(s)Z_o(s) - G_2(s)G_1(s) \tag{37}$$

F. Power in Unbalanced Systems

The apparent power (steady state) drawn from an unbalanced three-phase voltage source v_{abc} by an unbalanced current i_{abc} can be calculated using voltage phasors $\bar{V}_{abc}$ and current phasors $\bar{I}_{abc}$ for phases a, b, and c [23]:

$$\bar{S} = \bar{V}_a(\bar{I}_a)^* + \bar{V}_b(\bar{I}_b)^* + \bar{V}_c(\bar{I}_c)^* = P + jQ \tag{38}$$

where P and Q are the active and reactive power, respectively, and

$$P = 3V_+I_+\cos\gamma_+ + 3V_-I_-\cos\gamma_- + 3V_0I_0\cos\gamma_0 \tag{39}$$

$$Q = 3V_+I_+\sin\gamma_+ + 3V_-I_-\sin\gamma_- + 3V_0I_0\sin\gamma_0 \tag{40}$$

In (39) and (40), V and I are the voltage and current RMS values; subscripts +, −, and 0 stand for positive, negative, and zero sequences, respectively; and γ is the angle that the current is lagging behind the voltage (a different one for each sequence).

Using the voltage and current components obtained, when applying (12) to phase voltages and currents, P and Q can be written as:

$$P = v_d^+i_d^+ + v_d^-i_d^- + 2v_o^+i_o^+ + v_q^+i_q^+ + v_q^-i_q^- + 2v_o^-i_o^- \tag{41}$$

$$Q = v_q^+i_d^+ - v_q^-i_d^- + 2v_o^-i_o^+ + v_d^-i_q^- - v_d^+i_q^+ - 2v_o^+i_o^- \tag{42}$$

III. Microgrid Model and Dynamic Equations

A. Detailed GFo-VSC Model

VSCs consist of both active switching devices such as insulated-gate bipolar transistors (IGBTs) with pulse width modulation (PWM), and passive components such as LCL filters, to assist switching-harmonic filtering. In distributed generation (DG) systems, VSCs are generally used with effective switching frequencies above 10 kHz for low- and me-

dium-power applications. Therefore, converter switching can be averaged for small-signal stability analysis. In addition, if those converters are assumed to be fed from a sufficiently large DC power source, they can be modelled by ideal controllable three-phase voltage sources.

In this paper, GFo-VSCs have been controlled using an inner current control loop and an outer voltage control loop (see Fig. 4) to ensure that the converter output voltage closely tracks the desired set point (voltage modulus and frequency *V/f*) with both good transient and steady-state performances. Two-degree-of-freedom (2-DOF) proportional-integral (PI) controllers with independent reference weighting [24] have been used to control voltage and current components after the appropriate transformation from the three-phase description. The controller used for converter i is shown in (43) with controller parameters $K_{j,i}$, $b_{j,i}$, and $T_{j,i}$.

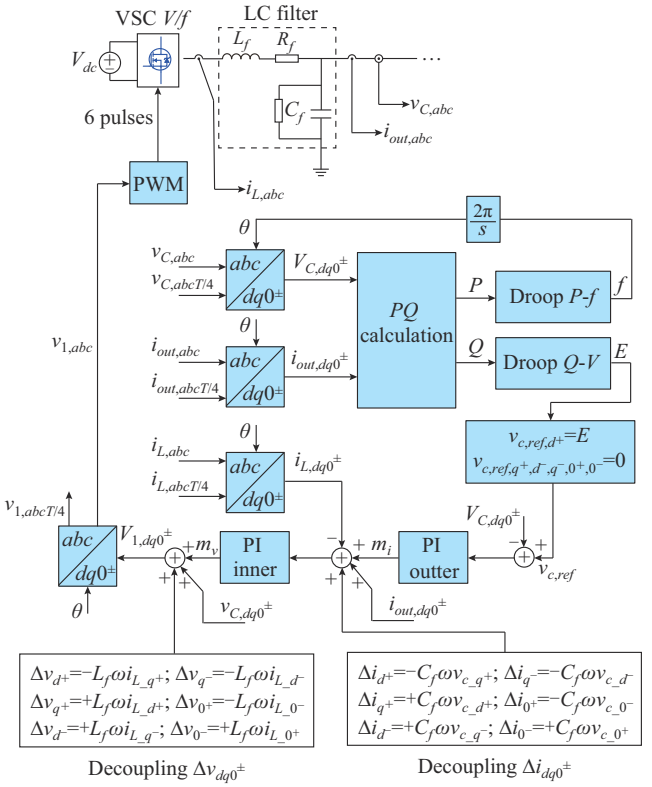

Fig. 4. *V/f* control of GFo-VSC.

$$M_{ji}(s)=K_{j,i}\left[\left(b_{j,i}+\frac{1}{T_{j,i}s}\right)R_{ji}(s)-\left(1+\frac{1}{T_{j,i}s}\right)Y_{ji}(s)\right] \tag{43}$$

where $M_{ji}(s)$ is the controller output; $R_{ji}(s)$ is the set-point input; and $Y_{ji}(s)$ is the process measured output for converter i (voltage when $j=2$ or current when $j=1$). Control details for the GFo-VSC, with the $\{dq0^{\pm}\}$ decoupling terms added to the controller outputs, are shown in Fig. 4. The decoupling terms shown extend the ones used in balanced cases such as those described in [7], among many others. In Fig. 4, *abc*/*dq*0$^{\pm}$ block is the modified Park's transformation in Section II-A. The *PQ* calculation block refers to (41) and (42). The droop *P-f* and droop *Q-V* blocks refer to the droop equations with first-order low-pass filter defined in Section III-B. L_f, R_f, and C_f model the VSC output LC filter. *out*, *ref*, *i*, and *v* stand for output, reference or set point, current, and voltage, respectively.

For the unbalanced-load case of interest in this paper, when only the positive sequence (dq^+) is considered in the internal controls of each GFo-VSC, the modal analysis shows a set of under-damped modes related with the inner current and outer voltage dynamics of their LC filters. This problem has been tackled by applying PI controllers such as in (43) to negative and zero ($dq^-0^{\pm}$) sequence currents and voltages, to keep the voltage balanced at their LC filter outputs, with $v^-_{d,ref}=v^-_{q,ref}=v^+_{0,ref}=v^-_{0,ref}=0$. Notice that this paper focuses on the stability analysis of unbalanced microgrids; however, if the interest were to compensate unbalanced currents and/or voltages using a GFo-VSC, the filter output voltage references need to be updated accordingly in the $v_{c,ref}$ block of Fig. 4, as in [25], for example.

B. Droop in GFo-VSCs

Primary control shapes the initial response of each generator when a disturbance takes place. At least one GFo-VSC converter will be required in any microgrid in island mode, and the following primary frequency and voltage control laws (i.e., droops) are usually proposed for each GFo-VSC$_i$:

$$\begin{cases}\Delta f_i=-K_{pi}\Delta P_i\\ \Delta V_i=-K_{qi}\Delta Q_i\end{cases} \tag{44}$$

where f_i is the output frequency; V_i is the output voltage; P_i and Q_i are the active and reactive power, respectively; ΔP_i and ΔQ_i are the differences between the set-point values and actual values measured at the GFo-VSC output; and K_{pi} and K_{qi} are the frequency- and voltage-droop gains, respectively.

Droop equations imitate, artificially, the behaviour of a traditional synchronous generator: when a generator's P load increases/decreases, the output frequency (generator's speed) decreases/increases; and, similarly, when the generator's Q load increases/decreases, the generator terminal voltage decreases/increases. In addition, droops in (44) rely on the fact that typical electrical grids and loads show a positive sensitivity in P and Q consumed with respect to frequency and voltage, respectively ($\Delta P/\Delta f>0$, $\Delta Q/\Delta V>0$); and therefore, (44) close control loops with negative feedback.

When GFo-VSCs are connected in parallel, droop gains K_{pi} and K_{qi} are usually selected by balancing VSC apparent power S ratings [26], in such a way that the VSC with the highest rating will be the one providing more power initially, towards a new equilibrium situation. Therefore,

$$\begin{cases}K_{pi}S_i=K_{pi+1}S_{i+1}\\ K_{qi}S_i=K_{qi+1}S_{i+1}\end{cases} \tag{45}$$

The noise in P and Q measurements can be filtered by applying first-order low-pass filters to the right-hand side of (44):

$$\tau_{f,i}\frac{\mathrm{d}\Delta f_i}{\mathrm{d}t}=-K_{pi}\Delta P_i-\Delta f_i \tag{46}$$

$$\tau_{V,i}\frac{\mathrm{d}\Delta V_i}{\mathrm{d}t}=-K_{qi}\Delta Q_i-\Delta V_i \tag{47}$$

where $\tau_{f,i}$ and $\tau_{V,i}$ are the time constants. A ΔP_i-filter can also be seen as the addition of a virtual inertia to VSC$_i$. In fact, [27] shows that if (46) is written in p.u., $K_{pi}=1/D_i$, and $\tau_{fi}=2H_i/D_i$, where D_i is the so-call damping coefficient of a converter i; and H_i is its virtual inertia in seconds. The actual damping of the resulting "swing equation" of a converter i connected to a reference bus is proportional to $D_i/\sqrt{H_i}$, and its natural frequency is proportional to $1/\sqrt{H_i}$.

C. Converter Angle Reference

One of the GFo-VSCs in the microgrid must be chosen to be the common reference for the "rotor angles" of all simulated generators. If the microgrid is stable, the system frequency will eventually reach a steady state value, and all state variables will be constant values in the new equilibrium point. If ω_0 is the output frequency of the reference converter, and ω_i is the output frequency of converter i, the relative "speed" of the latter with respect to the former can be written as follows:

$$\frac{\mathrm{d}\delta_i}{\mathrm{d}t}=\omega_i-\omega_0 \tag{48}$$

After a transient, the final frequency value will often not be equal to the base frequency till the secondary control level corrects the issue.

IV. Case Studies

A. Case Study 1: The Simplest System

First of all, the system in Fig. 5 has been analysed under balanced load and unbalanced load conditions using the transformation in (5) (with $\hat{\boldsymbol{T}}(t)$). It consists of: two GFo converters, i.e., VSC 1 and VSC 2, connected to Buses 1 and 2, respectively, through two transformers ($L_{dg1,2}, R_{dg1,2}$); a power line represented by (L_{line}, R_{Line}) between Buses 1 and 2; and two linear loads ($R_{1,2}, L_{1,2}$) connected to Buses 1 and 2 (differences will be explained for balanced and unbalanced cases). In addition, two very small capacitors (C_d) have been connected to Buses 1 and 2, to include the bus voltages as state variables. These capacitors should have no influence on the system dynamics, unless the line becomes very long. System parameters, base magnitudes, and controller (including droops) parameters are in Table IV. Note that $S_{base}=$ 35 kVA, $V_{base}=400$ V, $Z_{base}=V_{base}^2/S_{base}$, $f_{base}=50$ Hz, $V_{base}=Z_{base}I_{base}$, and pf is the load power factor. Controllers and droops have been described in Section III-A and III-B, respectively.

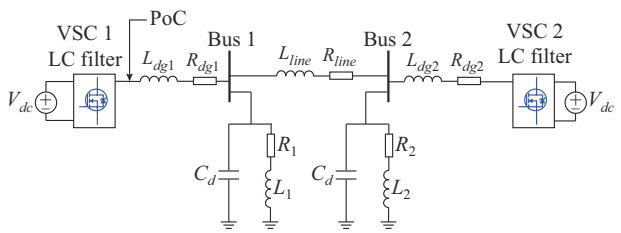

Fig. 5. Case study 1: single-line diagram where each VSC includes its LC filter.

GFo-VSC-1 has been assigned as the angle reference; therefore, its equivalent "rotor angle" is always zero. Under these circumstances, for simplicity, one can assume that the power delivered by GFo-VSC-2 is proportional to its rotor angle, i.e., $P_2\approx K_2\delta_2$, and the second-order differential equation that relates the power reference and the "rotor angle" has a natural frequency and a damping coefficient, as mentioned in Section III-B. Changing only the value of inertia H_i will alter both the bandwidth of the droop filter and the expected damping of the equivalent swing equation. A constant damping coefficient can be obtained if H_i and D_i are changed simultaneously, but the steady state frequency deviation will be affected.

TABLE IV
Parameters in Case Study 1

Component	Variable	Value	Component	Variable	Value
DG 1	S_1	1 p.u.	DG 2	S_2	0.7143 p.u.
	V_{1n}	1 p.u.		V_{2n}	1 p.u.
	K_{11}	11.79 p.u.		K_{12}	5.8844 p.u.
	T_{i11}	2.817×10^{-4} p.u.		T_{i12}	5.604×10^{-4} p.u.
	b_{11}	0.8905 p.u.		b_{12}	0.8922 p.u.
	K_{21}	0.7314 p.u.		K_{22}	0.3657 p.u.
	T_{i21}	7.88125×10^{-4} p.u.		T_{i22}	1.6×10^{-3} p.u.
	b_{21}	0.80 p.u.		b_{22}	0.80 p.u.
	R_{f1}	0.0219 p.u.		R_{f2}	0.0219 p.u.
	L_{f1}	0.1031 p.u.		L_{f2}	0.1031 p.u.
	C_{f1}	0.0287 p.u.		C_{f2}	0.0287 p.u.
	$\tau_{f,1}$	31.8 ms		$\tau_{f,2}$	31.8 ms
	$\tau_{V,1}$	31.8 ms		$\tau_{V,2}$	31.8 ms
Transformer (PT) 1	S_{t1}	0.5714 p.u.	PT 2	S_{t2}	0.5714 p.u.
	V_{n1}	1 p.u.		V_{n2}	1 p.u.
	Z_{dg1}	0.07 p.u.		Z_{dg2}	0.07 p.u.
	X/R	0.5 p.u.		X/R	0.5 p.u.
Bus 1	C_{d1}, C_{d2}	1.436×10^{-9} p.u.	Bus 2	C_{d1}, C_{d2}	1.436×10^{-9} p.u.
Line	Distance	140 m	Load 1	S_{l1}	0.5143 p.u.
	R_{line}	0.0252 p.u.		pf_1	0.85 p.u.
	L_{line}	0.0026 p.u.	Load 2	S_{l2}	0.3429 p.u.
	$\rho_{line}=X_L/R$	0.103 p.u.		pf_2	0.85 p.u.

Modal analysis considering all state variables in the system has been carried out with varying K_{pi} or τ_{fi} in two ways: ① independently; and ② by trying to maintain a constant damping coefficient of the equivalent swing equation. Results of the modal analysis will be compared with those using the impedance-based approach to study stability. Only the case of single-phase loads (connecting phase a to ground) in Buses 1 and 2 will be reported for the unbalanced case.

1) Under Balanced Load

The system in Fig. 5 has balanced three-phase star-connected loads with the neutral connected to ground, although in this case the neutral current is always zero. It corresponds to a 35$^{\text{th}}$-order system using conventional Park's transforma-

tion (3) under balanced conditions. Variable names are associated to numbers in Table V. Once linearised, the system has 35 distinct eigenvalues (modes).

TABLE V
ELEMENTS, AND VARIABLE NAMES AND NUMBERS

Type	Element	Variable	Number
With balanced load	Load 1	i_{dq}	1, 2
	Load 2	i_{dq}	3, 4
	Line	i_{dq}	5, 6
	Bus capacitor	v_{dq}	7, 10
	f-droop		VSC 1: 11, VSC 2: 23
	V-droop		VSC 1: 12, VSC 2: 24
	Angle		VSC 2: 25
	PT	i_{dq}	VSC 1: 13, 14, VSC 2: 26, 27
	LC	v_{dq}	VSC 1: 15, 16, VSC 2: 28, 29
	LC	i_{dq}	VSC 1: 17, 18, VSC 2: 30, 31
	PI	i_{dq}	VSC 1: 19, 20, VSC 2: 32, 33
	PI	v_{dq}	VSC 1: 21, 22, VSC 2: 34, 35
With unbalanced load	1-phase load 1	i^{+}_{dq}	1-2
	1-phase load 2	i^{+}_{dq}	3-4
	Line	$i^{\pm}_{dq0}$	17-22
	Bus capacitor	$v^{\pm}_{dq0}$	5-16
	f-droop		VSC 1: 23, VSC 2: 55
	V-droop		VSC 1: 24, VSC 2: 56
	Angle		VSC 2: 57
	PT	$i^{\pm}_{dq0}$	VSC 1: 25-30, VSC 2: 58-63
	LC	$v^{\pm}_{dq0}$	VSC 1: 31-36, VSC 2: 64-69
	LC	$i^{\pm}_{dq0}$	VSC 1: 49-54, VSC 2: 82-87
	PI	$i^{\pm}_{o}$	VSC 1: 37, 38, VSC 2: 70, 71
	PI	i^{-}_{dq}	VSC 1: 41, 42, VSC 2: 74, 75
	PI	i^{+}_{dq}	VSC 1: 45, 46, VSC 2: 78, 79
	PI	$v^{\pm}_{o}$	VSC 1: 39, 40, VSC 2: 72, 73
	PI	v^{-}_{dq}	VSC 1: 43, 44, VSC 2: 76, 77
	PI	v^{+}_{dq}	VSC 1: 47, 48, VSC 2: 80, 81

The participation factors of those eigenvalues in the system state variables is described in Fig. 6. The state variable indices on the *y*-axis correspond to the variable numbers in Table V (balanced load). The eigenvalue (mode) index corresponds to a list ordered from the slowest one to the fastest one, considering the eigenvalue real parts. A coloured point has been added when one of the 35 eigenvalues in the *x*-axis has a relevant participation in one of the 35 state variables in the *y*-axis. The coloured column in the figure quantifies the participation factor from 0 (no participation) in dark blue, to 1 (maximum) in red. For example, modes $\{1,2\}$ participate in state variables $\{11,23,25\}$, which correspond to the frequency-droop filters of VSC 1 and VSC 2, and the angle dynamics of VSC 2, respectively (see Table V).

The modal analysis in Fig. 6 can be further validated by comparing the free responses of the linearised system from its initial conditions applying (30) and (31), with the corresponding perturbation responses of the original non-linear system. For example, the angle and the *d*-axis component of the LC capacitor voltage for VSC 2, have been compared for the linearised and non-linear systems, with a small perturbation in the angle of VSC 2 at $t=2$ s, as shown in Figs. 7 and 8. Notice that the initial time and the equilibrium-point value of the non-linear responses have been subtracted in order to be better compared with the linear free responses.

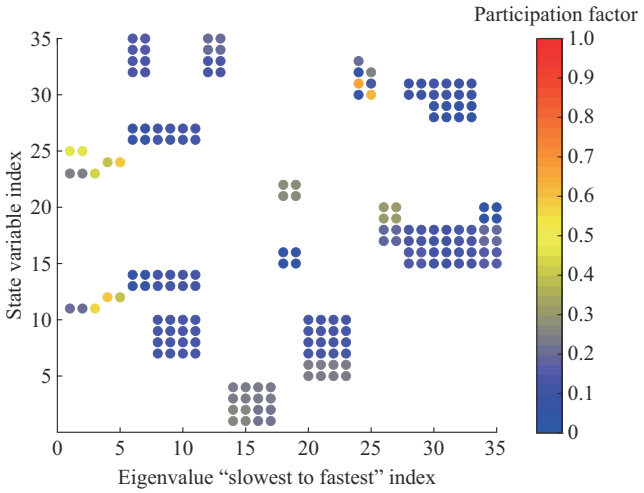

Fig. 6. Participation factors for $D_1=54.94$ and $H_1=0.87$ s (droop constants in Table IV).

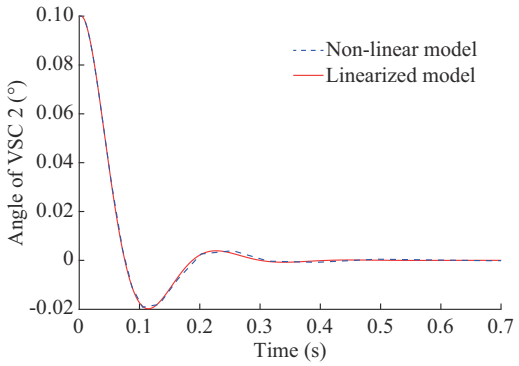

Fig. 7. Validation test: angle of VSC 2 in non-linear system response, and in linear system free response when a small perturbation in angle of VSC 2 is applied ($\Delta\delta_2=x_{25}(0)=0.1°$).

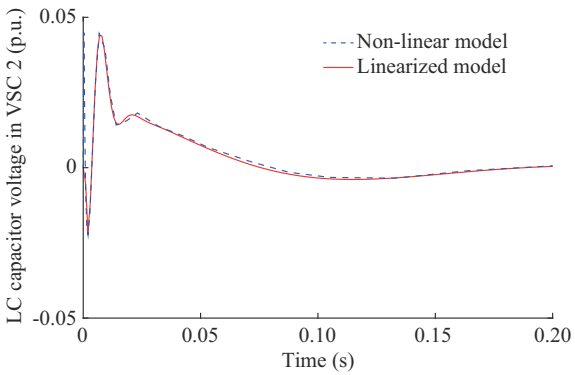

Fig. 8. Validation test: LC capacitor voltage (*d*-axis) in VSC 2 in non-linear system response, and in linear system free response when a small perturbation in angle of VSC 2 is applied ($\Delta\delta_2=x_{25}(0)=0.1°$).

When the converter frequency-droop gains K_{pi} increase, the eigenvalues of the linearised system move as shown in

Fig. 9 (see colour bar for gain variations). Moduli of eigenvalues $w=|\lambda_i|$ are in the x-axis with a logarithmic scale, so that large and small eigenvalues can be represented together. Damping coefficients of eigenvalues ($\zeta=-\mathrm{Re}(\lambda_i)/|\lambda_i|$) are in the y-axis with a linear scale. The numbers within the graph refer to the position of the eigenvalue in the x-axis of Fig. 6.

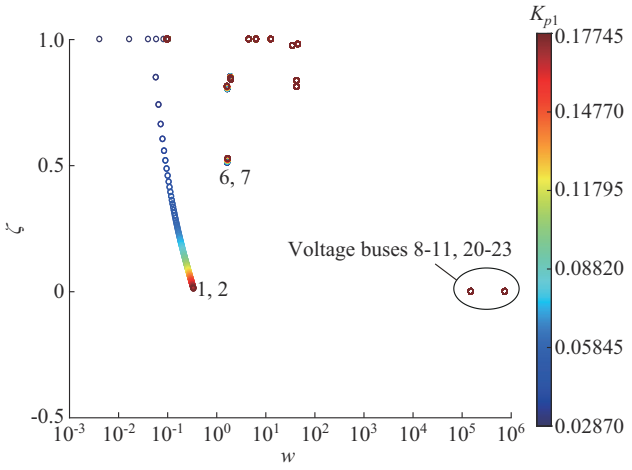

Fig. 9. System modes' loci when frequency-droop gains increase.

For example, λ_8-λ_{11} and λ_{20}-λ_{23} have very large moduli and participate in the state variables related to the bus capacitors (variables 7-10), transformer 1 (variables 13, 14), transformer 2 (variables 26, 27), and the line (variables 5, 6). Figure 9 also shows that if parameters K_{pi} increase, the moduli of complex conjugated λ_1 and λ_2 grow, while their damping coefficients deteriorate, reaching instability when droop gains are $K_{p1}=0.2037$ and $K_{p2}=0.2855$. Those eigenvalues participate in the state variables of the frequency-droop filters and the angle dynamics of GFo-VSC-2 (variables 11, 23, and 25). No other eigenvalue moves significantly.

Figure 10 shows how eigenvalues move when the time constants of the frequency-droop filters τ_{fi} are increased. All eigenvalues which participate in droop filter variables reduce their moduli, and damping coefficients of numbers 1 and 2 deteriorate. In order to maintain a constant damping coefficient in the equivalent swing equation, parameters H_i and D_i of the frequency droops will have to be changed simultaneously, as shown in Fig. 11.

The stability of the system in Fig. 5 has also been examined by applying the impedance-based procedure using the open-loop transfer function $L(s)$ in (37). In balanced systems, the loci of the two eigenvalues of the transfer function $L(s)$ must be considered. However, a clearer picture is obtained by a single graph with the locus of the determinant of $[I+L(s)]$ and its encirclements of the origin $(0,0)$ as s goes clockwise around the right-hand side of the complex plane. Since there is no unstable poles of $L(s)$, the locus of the determinant will produce clockwise encirclements of the origin $(0,0)$ when the system becomes unstable [28]. This situation is reached for droop gains $K_{p1}>0.2037$ and $K_{p2}>0.2855$, and the limit case (already unstable) is shown in Fig. 12, where the locus steps on $(0,0)$. The locus goes through 1, 2, …, 8, as s goes clockwise around the righ-hand side complex plane.

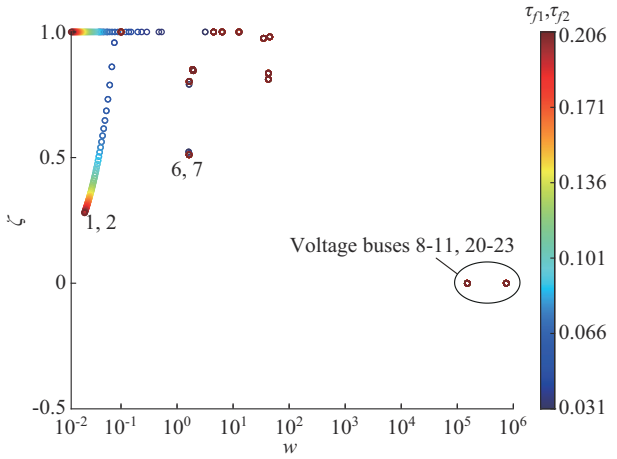

Fig. 10. System modes' loci when time constants of frequency-droop filters are increased.

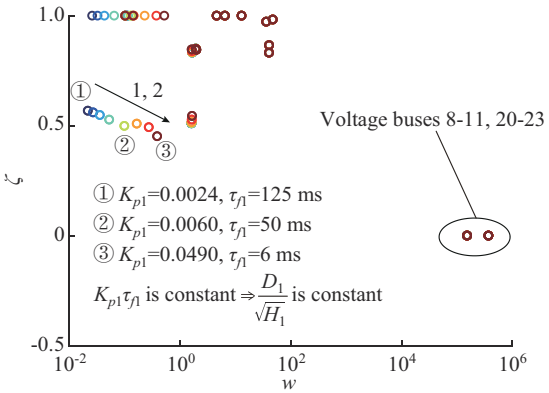

Fig. 11. Systems modes' loci changing frequency-droop filter parameters and maintaining a constant equivalent damping factor.

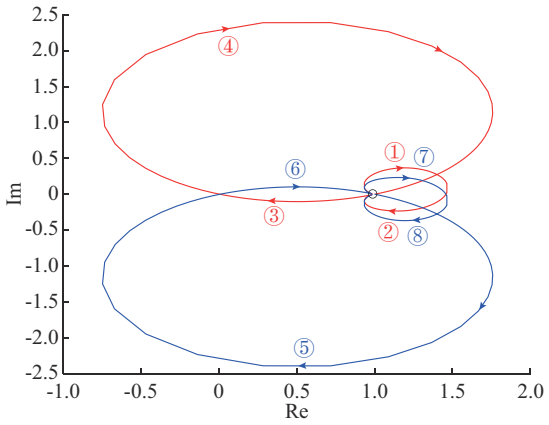

Fig. 12. Locus of det$[I+L(s)]$ with "almost" two clockwise encirclements of origin for droop gains $K_{p1}=0.2037$ and $K_{p2}=0.2855$ (unstable system).

2) *Under Unbalanced Load*

The system in Fig. 5 has also been analysed with single-phase loads connecting phase a to ground (as defined in Table IV) in Buses 1 and 2. Now, the system using the pro-

posed transformation described in Section II has 87 state variables and 87 distinct modes (once linearised). The participation of those eigenvalues in the system state variables is described in Fig. 13 following the strategy of Fig. 6. The variable indices on the *y*-axis are related with the system elements as indicated in Table V. In Fig. 13, the indices on the *y*-axis correspond to the variable number in Table V (unbalanced load). The eigenvalue (mode) index corresponds to a list ordered from the slowest one to the fastest one, considering the eigenvalue real parts.

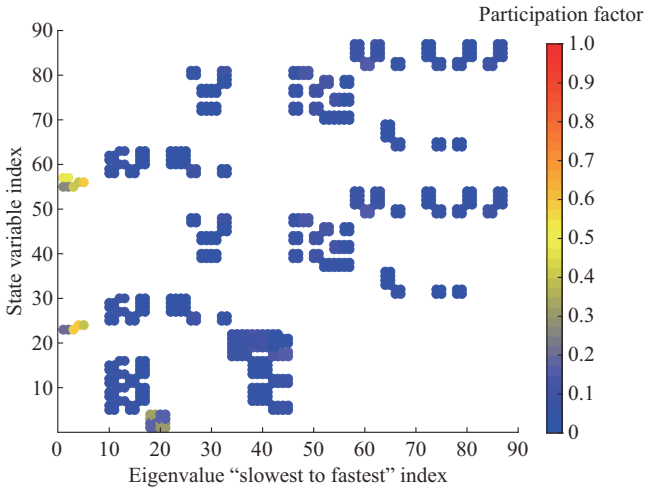

Fig. 13. Participation factors for $D_1=54.94$ and $H_1=0.87s$ (droop constants in Table IV).

First of all, the frequency-droop gains have been increased and the system modes' loci are shown in Fig. 14. Clearly, the damping factors of modes 1-2 deteriorate (they participate in the state variables of the frequency-droop filters and the angle of GFo-VSC-2), becoming unstable for $K_{p1}=0.228$ and $K_{p2}=0.321$.

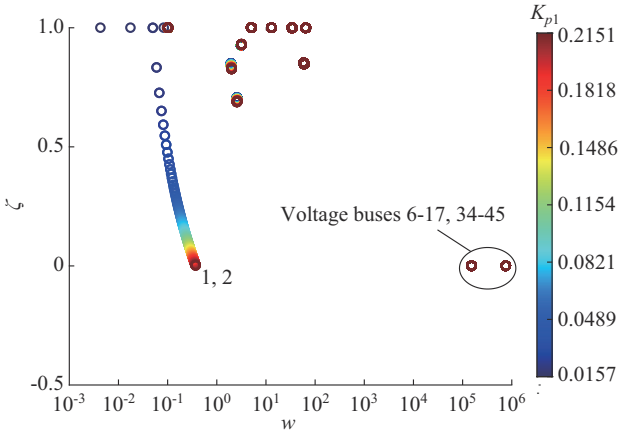

Fig. 14. System modes' loci when frequency-droop gains are increased.

Secondly, the time constants of the frequency-droop filters τ_{fi} are increased, while droop gains are maintained constant. All eigenvalues which participate in droop filter variables reduce their moduli, and the damping coefficients of eigenvalues 1 and 2 deteriorate. The loci of the system modes in this case have been drawn in Fig. 15. A constant damping coefficient in the equivalent swing equation can be maintained if parameters H and D of the frequency droops are changed simultaneously.

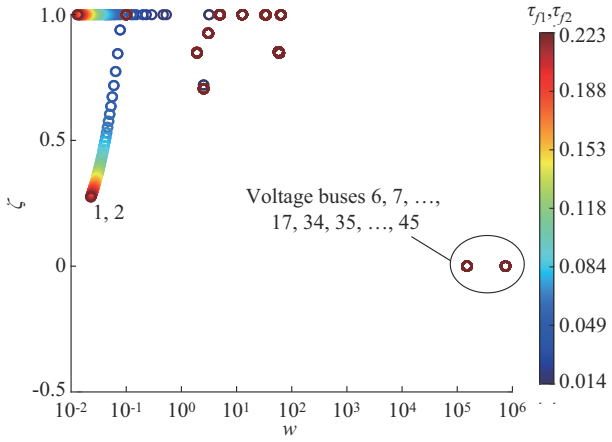

Fig. 15. System modes' loci when time constants of frequency-droop filters are increased.

In the unbalanced case, the impedance-based approach to study stability must handle 6×6 impedance matrices like the one in (28). As in the balanced case, the system will be unstable when det$[I+L(s)]$ produces clockwise encirclements of the origin as s goes clockwise around the right-hand side complex plane [28] (i.e., $K_{p1}>0.228$ and $K_{p2}>0.321$) and the limit case (already unstable) is shown in Fig. 16. The locus goes through $1, 2, \ldots, 8$ as s goes clockwise around the right-hand side complex plane.

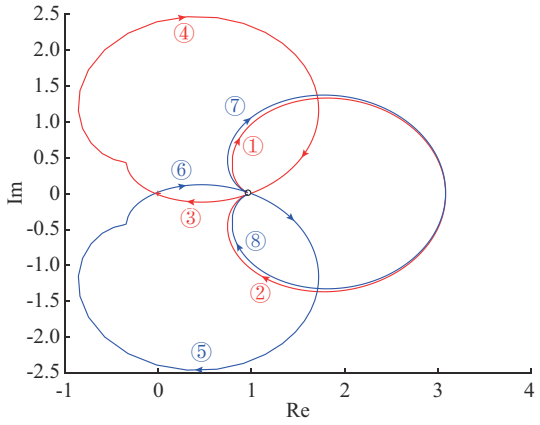

Fig. 16. Locus of det$[I+L(s)]$ for droop gains $K_{p1}=0.228$ and $K_{p2}=0.321$.

Finally, if the internal PI controllers for the negative sequence of GFo-VSC-2 defined in (43) are gradually removed, the system modes change as shown in Fig. 17. As gains K_{12} (inner current control) and K_{22} (outer voltage control) are reduced, the damping coefficients of the following set of modes deteriorate:

1) Modes $\{2, 3, 8, 9\}$ participate in state variables $\{76, 77\}$, $\{74, 75\}$ and $\{85, 86\}$, which are related with the negative sequence for: the PI voltage control, the PI current control, and the currents of the LC filter in GFo-VSC-2, respectively.

2) Modes $\{54, 55, \ldots, 57\}$ participate in state variables

{67, 68}, {85, 86}, {61, 62}, and {28, 29}, which are related with the negative sequence for the output voltage of the LC filter in GFo-VSC-2, the currents of the LC filter in GFo-VSC-2, and the currents of transformers 2 and 1, respectively.

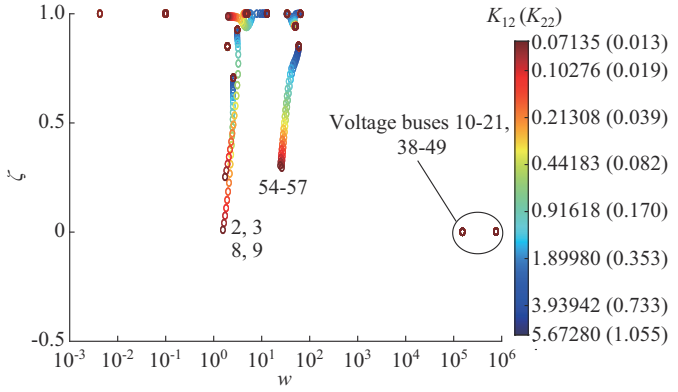

Fig. 17. System modes' loci when negative-sequence internal controls are removed at GFo-VSC-2.

Similar results have been obtained when removing the internal PI controllers corresponding to the zero sequence in GFo-VSC-2, showing an insignificant coupling between controllers of the positive, negative, and zero sequences.

B. Case Study 2: Complete LV CIGRE Microgrid

The complete low-voltage (LV) CIGRE unbalanced AC microgrid [15] in Fig. 18 has also been analysed. It consists of five GFo-VSCs connected to their buses through transformers (with impedances Z_{dg} as those in Section IV-A), ten balanced LV power lines (basic line impedances Z_{line} as the one in Section IV-A), and five linear unbalanced loads connected to their corresponding buses. In addition, eleven very small three-phase balanced capacitors C_d have been connected to the grid buses to include the bus voltages as state variables. These capacitors should have no influence on the system dynamics. All parameters are presented in Table IV.

GFo-VSC-1 is chosen to be the angle reference for all other converters and has the configuration of VSC 1 in Table IV while all other VSCs have identical configuration as VSC 2 in that table. The unbalanced loads are described in Table VI. They are three-phase star-connected loads with the neutral point connected to ground.

The complete CIGRE unbalanced microgrid is a 316th-order system, which, once linearized, has 316 distinct eigenvalues (modes) that participate in the system state variables. Two scenarios have been analysed: ① the case of removing the transformer at VSC 2; and ② the case when frequency-droop gains K_{pi} are increased.

1) Removing Transformer at VSC 2

The system modes' loci is shown in Fig. 19 when the impedance Z_{dg2} of transformer at VSC 2 is reduced gradually (maintaining the ratio *X/R*). The damping coefficients of a set of modes deteriorate:

1) Modes {1, 2} participate in state variables {187}, {185}, {284}, and {286}, which are related with the angle of VSC 2, the frequency-droop filter of VSC 2, the frequency-droop filter of VSC 5, and the angle of VSC 5, respectively.

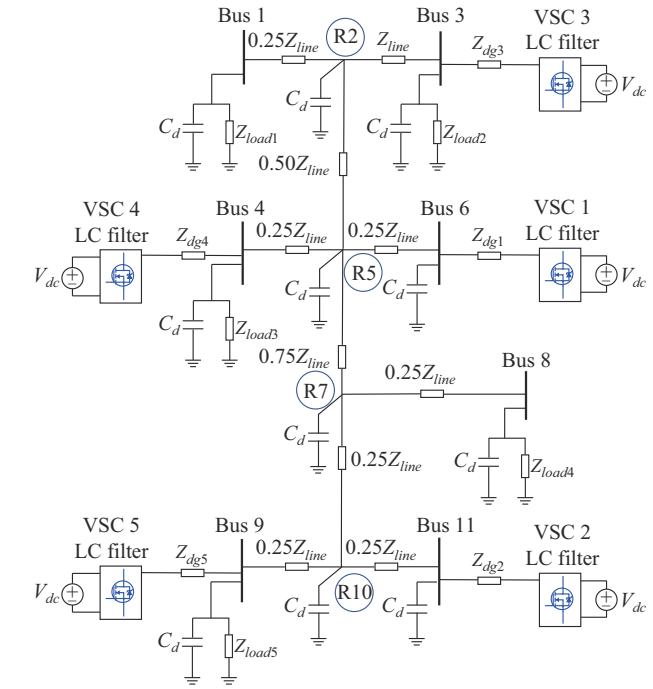

Fig. 18. Single-line diagram of LV CIGRE unbalanced AC microgrid where VSCs include LC filters.

TABLE VI
LOAD PARAMETERS IN CASE STUDY 2 (BASE VALUES AS IN TABLE IV)

Load (p.u.)	S_a	S_b	S_c	*pf*
1	0.0286	0.0571	0.0771	0.85
2	0.1371	0.1829	0.2286	0.85
3	0.1371	0.1829	0.2286	0.85
4	0.0771	0	0	0.85
5	0.0457	0.0914	0.1143	0.85

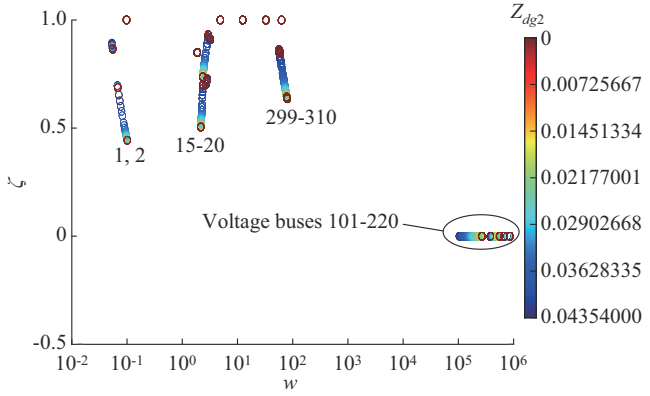

Fig. 19. Loci of eigenvalues in CIGRE microgrid when tranformer 2 is removed gradually.

2) Modes {15, 16, …, 20} participate in state variables {200, 201, …, 211}, which are related with the PI controllers of positive, negative, and zero sequences of voltages and currents in VSC2; in state variables {287, 288, …, 292}, which are related to the current at the transformer of VSC 5; and in state variables {307, 308, …, 310}, which are related with positive current and voltage PI control of VSC 5.

3) Modes {299, 300, …, 310} participate in state variables

{212, 212, …, 217} and {194, 195, …, 199}, which are related with the current and voltage of the LCL filter in VSC 2, respectively.

Last findings indicate that transformers help to maintain a better damping in the modes, and special care should be taken for possible interactions between nearby VSCs in the microgrid.

2) Increasing Frequency-droop Gains

The loci of eigenvalues of CIGRE microgrid when frequency-droop gains are increased are shown in Fig. 20. This time, when those gains are increased, the damping coefficients of modes {1, 2, …, 8} deteriorate and nearby VSCs exhibit interactions:

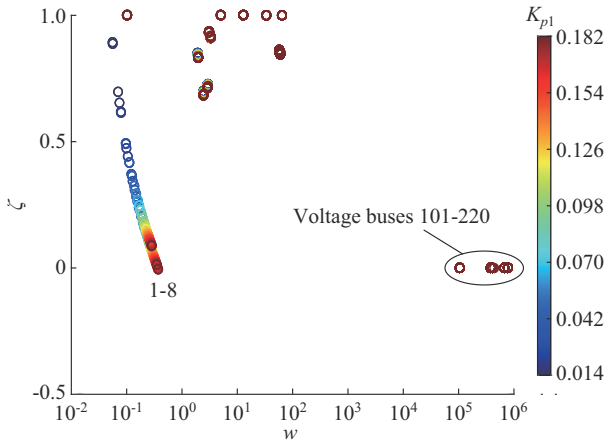

Fig. 20. Loci of eigenvalues of CIGRE microgrid when frequency-droop gains are increased.

1) Modes {1, 2} participate in state variables {185}, {187}, {284}, and {286}, which are related with the frequency-droop filter of VSC 2, the angle of VSC 2, the frequency-droop filter of VSC 5, and the angle of VSC 5, respectively.

2) Modes {3, 4} participate in state variables {153}, {251}, and {253}, which are related with the frequency-droop filter of VSC 1, the frequency-droop filter of VSC 4, and the angle of VSC 4, respectively.

3) Modes {5, 6} participate in state variables {153}, {185}, {187}, {284}, and {286}, which are related with the frequency-droop filter of VSC 1, the frequency-droop filter of VSC 2, the angle of VSC 2, the frequency-droop filter of VSC 5, and the angle of VSC 5, respectively.

4) Modes {7, 8} participate in state variables {218} and {220}, which are related with the frequency-droop filter of VSC 3 and the angle of VSC 3, respectively.

The slow dynamics caused by the frequency droops, show interaction among all five VSCs. However, a stronger interaction is revealed between VSC 2 and VSC 5, and between VSC 1 and VSC 4, due to the low line impedance between them, as shown in Fig. 18.

V. Conclusion

The proposed transformation from a three-phase system to a $\{dq0^{\pm}\}$ model provides a reliable tool for stability analysis in LVAC microgrids under unbalanced conditions. Naturally, modal analysis and the impedance-based method reveal the same final conclusions when analysing the stability of a simple case, because they are both based on a small-signal linear approximation of the system. The former requires a detailed model of every single element of the system, while the latter could be applied with a simpler equivalent model which can be derived experimentally at the PoC. However, the former gives a richer insight into the system behaviour than the latter.

The paper has shown how the parameters of the filter used to measure active power in a typical frequency droop would affect the stability of a simple microgrid based on GFo-VSCs and how these parameters are clearly related to the damping D and the inertia H of the so-called "virtual inertia" provided by GFo-VSCs. The paper has also illustrated how these two parameters must be changed together in order to maintain an approximately constant damping coefficient in the equivalent "swing equation" of the system. Although this equation is only an approximation, the detailed modal analysis of the system reveals that, with the proposed strategy, the damping coefficients of those modes remain almost constant with a strong participation in the frequency-droop state variables and in the VSC angle. The modal analysis applied to an unbalanced system has unveiled the importance of the dynamics in the $\{dq^{-}\}$ and $\{0^{\pm}\}$ components, which have to be closed-loop controlled in order to improve the system stability.

Finally, the analysis conducted in the complete CIGRE microgrid indicates that the transformers used to connect GFo converters provide galvanic isolation and a better damping response in the overall dynamics of the system. Due to the high number of modes in the complete microgrid, an adequate model reduction technique should be considered to focus on the most relevant modes.

References

[1] J. Rocabert, A. Luna, F. Blaabjerg *et al.*, "Control of power converters in AC microgrids," *IEEE Transactions on Power Electronics*, vol. 27, no. 11, pp. 4734-4749, May 2012.

[2] P. Kundur and L. Wang, "Small signal stability analysis: experiences, achievements, and challenges," in *Proceedings of International Conference on Power System Technology*, Kunming, China, Oct. 2002, pp. 6-12.

[3] F. Pagola, I. Perez-Arriaga, and G. Verghese, "On sensitivities, residues and participations: applications to oscillatory stability analysis and control," *IEEE Transactions on Power Systems*, vol. 4, no. 1, pp. 278-285, Feb. 1989.

[4] J. Paseba, "Control of power system oscillations," in *Proceedings of IFAC Symposium on Control of Power Systems and Power Plants*, Beijing, China, Aug. 1997, pp. 75-83.

[5] L. Rouco, "Coordinated design of multiple controllers for damping power system oscillations," *International Journal of Electrical Power & Energy Systems*, vol. 23, pp. 517-530, Oct. 2001.

[6] J. Renedo, A. Garcia-Cerrada, L. Rouco *et al.*, "Coordinated design of suplementary controllers in VSC-HVDC multi-terminal systems to damp electromecanical oscillations," *IEEE Transactions on Power Systems*, vol. 36, no. 1, pp. 712-721, Jan. 2021.

[7] N. Pogaku, M. Prodanović, and T. C. Green, "Modeling, analysis and testing of autonomous operation of an inverter-based microgrid," *IEEE Transactions on Power Electronics*, vol. 22, no. 2, pp. 613-625, Mar. 2007.

[8] Z. Li and M. Shahidehpour, "Small-signal modeling and stability analysis of hybrid AC/DC microgrids," *IEEE Transactions on Smart Grid*, vol. 10, no. 2, pp. 2080-2095, Mar. 2019.

[9] Y. Yan, D. Shi, D. Bian *et al.*, "Small-signal stability analysis and per-

formance evaluation of microgrids under distributed control," *IEEE Transactions on Smart Grid*, vol. 10, no. 5, pp. 4848-4858, Sept. 2018.
[10] D. P. Ariyasinghe, D. M. Vilathgamuwa, and S. Member, "Stability analysis of microgrids with constant power loads," in *Proceedings of International Conference on Sustainable Energy Technologies*, Singapore, Nov. 2008, pp. 279-284.
[11] IEEE PES Task Force on Microgrid Stability Analysis and Modeling, "Microgrid stability definitions, analysis, and modeling," Tech. Rep. no. PES-TR 66, Jun. 2018.
[12] M. Farrokhabadi, D. Lagos, R. W. Wies *et al*., "Microgrid stability definitions, analysis, and examples," *IEEE Transactions on Power Systems*, vol. 35, no. 1, pp. 13-29, Jan. 2020.
[13] Y. Ojo and J. Schiffer, "Towards a time-domain modeling framework for small-signal analysis of unbalanced microgrids," in *Proceedings of IEEE PowerTech Conference*, Manchester, UK, Jun. 2017, pp. 1-6.
[14] B. S. Shah, P. Koralewicz, V. Gevorgian *et al*., "Impedance methods for analyzing the stability impacts of inverter-based resources," *IEEE Electrification Magazine*, vol. 9, no. 1, pp. 53-65, Mar. 2021.
[15] CIGRE Task Force C6.04.02, "Benchmark systems for network integration of renewable and distributed energy resources," CIGRE Tech. Rep. No. 575, Apr. 2014.
[16] G. Verghese, I. Perez-Arriaga, and F. Schweppe, "Selective modal analysis with applications to electric power systems, Part I: heuristic introduction and Part II : the dynamic stability problem," *IEEE Transations on Power Apparatus and Systems*, vol. PAS-101, no. 9, pp. 3117-3134, Sept. 1982.
[17] F. Milano, *Power System Modelling and Scripting*, 1st ed., Berlin: Springer Publishing Company, Aug. 2010.
[18] R. Middlebrook, "Input filter considerations in design and application of switching regulators," in *Proceedings of IEEE Industry Applications Society Annual Meeting*, Chicago, USA, Oct. 1976, pp. 366-382.
[19] M. Belkhayat, "Stability criteria for AC power systems with regulated loads," Ph. D. dissertation, Purdue University, West Lafayette, USA, 1997.
[20] A. G. J. Macfarlane and I. Postlethwaite, "The generalized nyquist stability criterion and multivariable root loci," *International Journal of Control*, vol. 25, no. 1, pp. 81-127, Jun. 1977.
[21] B. Wen, D. Boroyevich, R. Burgos *et al*., "Small-signal stability analysis of three-phase AC systems in the presence of constant power loads based on measured *d-q* frame impedances," *IEEE Transactions on Power Electronics*, vol. 30, no. 10, pp. 5952-5963, Oct. 2015.
[22] Z. Liu, J. Liu, D. Boroyevich *et al*., "Stability criterion of droop-controlled parallel inverters based on terminal-characteristics of individual inverters," in *Proceedings of 2016 IEEE 8th International Power Electronics and Motion Control Conference*, Hefei, China, May 2016, pp. 2958-2963.
[23] J. D. Glover, M. S. Sarma，and T. H. Overbye, *Power System Analysis and Design*, 4th ed., Ontario: Thomson Learning, 2012.
[24] K. J. Åström and T. Hägglund, *PID Controllers: Theory, Design, and Tuning*, 2nd ed., Research Triangle Park: Instrument Society of America, 1995.
[25] M. Savaghebi, A. Jalilian, J. C. Vasquez *et al*., "Autonomous voltage unbalance compensation in an islanded droop-controlled microgrid," *IEEE Transactions on Industrial Electronics*, vol. 60, no. 4, pp. 1390-1402, Apr. 2013.
[26] M. C. Chandorkar, D. M. Divan, and R. Adapa, "Control of parallel connected inverters in standalone AC supply systems," *IEEE Transactions on Industry Applications*, vol. 29, no. 1, pp. 136-143, Jan.-Feb. 1993.
[27] R. Ofir, U. Markovic, P. Aristidou *et al*., "Droop vs. virtual inertia: comparison from the perspective of converter operation mode," in *Proceedings of 2018 IEEE International Energy Conference*, Limassol, Cyprus, Jun. 2018, pp. 1-6.
[28] C. A. Desoer and Y. Wang, "On the generalized Nyquist stability criterion," *IEEE Transactions on Automatic Control*, vol. 25, no. 2, pp. 187-196, Apr. 1980.

Sauro J. Yague received the M.Sc. degree from ICAI School of Engineering, Comillas Pontifical University, Madrid, Spain, and another M. Sc. degree in electrical engineering from Wichita State University, Kansas, USA, in 1996 and 1998, respectively. Currently, he is a Professor at IQS School of Engineering, Ramón Llull University, Barcelona, Spain. His research interests include power electronics and its applications to electric energy systems.

Aurelio García-Cerrada received the M. Sc. degree from the Universidad Politécnica de Madrid, Madrid, Spain, and the Ph.D. degree from the University of Birmingham, Birmingham, U.K., in 1986 and 1991, repectively. He is a Professor in the Electronics, Control Engineering and Communications Department and a Member of the Institute for Research in Technology at the Universidad Pontificia Comillas de Madrid, Madrid, Spain. His research interests include power electronics and its applications to electric energy systems.

Pere Palacín Farré received the M. Sc. degree from the Universidad Politécnica de Cataluña, Barcelona, Spain, in 1992, and the Ph. D. degree from the Universidad Ramón Llull, Barcelona, Spain, in 2005. He has been General Director of Energy, Mines, and Industrial Security at the Generalidad de Cataluña (2013-2020), Vice-president of the Instituto de Energía-ICAEN (2013-2018), and Dean of the Colegio Oficial de Ingenieros Industriales de Cataluña-COEIC (2017). Currently, he is a Professor at IQS School of Engineering, Ramón Llull University, Barcelona, Spain. His research interests include power systems, microgrids, smart grids, and renewable energies.